Gonen, S., Pulatsu, B., Erduran, E., Pelà, L., Soyoz, S. (2024) "Dynamic Characteristics of Stone Masonry Walls Before and After Damage: Experimental and Numerical Investigations", *Engineering Structures*, 306, 117808. https://doi.org/10.1016/j.engstruct.2024.117808

Dynamic Characteristics of Stone Masonry Walls Before and After Damage: Experimental and Numerical Investigations

Semih Gonen[1*], Bora Pulatsu[2], Emrah Erduran[3], Luca Pelà[1], and Serdar Soyoz[4]

Abstract: Seismic behavior of masonry walls has been heavily investigated, especially by means of laboratory experiments employing cyclic tests to determine the mechanical parameters and seismic capacity. Nevertheless, the dynamic properties of the tested walls often remain unknown, even though the nature of the seismic response is dynamic and profoundly affected by the structure's dynamic properties. This paper presents an investigation on the dynamic properties of three different masonry wall panels in healthy and damaged states, and examines if damage quantification via tracking the changes in dynamic properties is feasible. Ambient vibration and impact measurements are used for the dynamic identification of wall panels, before and after they are tested in reversed-cyclic in-plane shear-compression tests. The natural frequencies, damping ratios, and mode shapes of the walls are determined and compared to each other. Moreover, the damage progression and its effect on the dynamic features of URM wall panels is investigated using a discrete element model of the benchmark wall that is validated in terms of the force-displacement response and damage pattern of the wall. The results of the study indicate that changes in natural frequencies and mode shapes are traceable, although it is difficult to infer damage quantification relationships from these changes. The outcomes of this study also highlight that numerical models verified with the nonlinear quasi-static behavior do not necessarily match the wall´s dynamic behavior, and that more research is required to update nonlinear numerical models. Overall, the results contribute to the knowledge regarding the dynamic characteristics of masonry walls in healthy and damaged conditions, and to quantify the damage in masonry walls as well as the changes in their dynamic properties.

Keywords: Stone-masonry wall, System identification, Seismic damage quantification, Non-destructive inspection, Discrete element method, Ambient vibrations

1 Department of Civil and Environmental Engineering, Universitat Politècnica de Catalunya (UPC-BarcelonaTech), C/ Jordi Girona, 1-3, Barcelona, 08034, Spain
2 Department of Civil and Environmental Engineering, Carleton University, Ottawa, ON K1S 5B6, Canada
3 Department of Built Environment, Oslo Metropolitan University, Oslo, Norway
4 Department of Civil Engineering, Bogazici University, Bebek, Istanbul, Turkiye
* corresponding author, semih.gonen@upc.edu

Gonen, S., Pulatsu, B., Erduran, E., Pelà, L., Soyoz, S. (2024) "Dynamic Characteristics of Stone Masonry Walls Before and After Damage: Experimental and Numerical Investigations", *Engineering Structures*, 306, 117808. https://doi.org/10.1016/j.engstruct.2024.117808

Highlights

- Cyclic shear-compression tests on three stone masonry wall panels
- Dynamic identification in healthy state and after damage
- Effects of damages on the dynamic properties of the walls
- Effects of strengthening on the dynamic properties of the walls
- Numerical investigation of modal properties in healthy and damaged states

1 Introduction

Masonry structures have a profound place in the existing building stock, especially in earthquake-prone regions such as Italy, Greece, Portugal, and Turkey. Past and recent earthquakes demonstrated that, unless strengthened or reinforced, masonry buildings are vulnerable to seismic loads due to weak bond strength properties in tension and shear, lack of connection between the orthogonal walls as well as the slab and walls, and due to improper interventions, among many other factors. Owing to the widespread use and vulnerability of unreinforced masonry, the seismic behavior of masonry structures has received significant attention in the last decades [1–11]. Masonry wall panels representing a specific structural part of various structure typologies, such as buildings, retaining walls, monumental structures, and arch bridges, have been extensively tested in laboratories by several researchers. The recent experimental findings on the cyclic behavior of masonry walls suggest that several parameters considerably affect the in-plane behavior of masonry walls. Amongst those, the size effect and aspect ratio [12–14], the boundary conditions [15,16], the loading protocol [16,17], and the pre-compression level [13,18–20] can be pointed out as examples. The cyclic tests have enabled determining the seismic resistance and related parameters such as ductility, energy absorption capacity, and strength and stiffness degradation [16,21]. Meanwhile, dynamic properties of the tested walls, such as mode shapes and natural frequencies, and how they alter with damage remained unexplored, as typically they are not the primary information sought. Nevertheless, they can provide crucial information to develop a simple and reliable technique to assess the current condition of the walls, allowing the implementation of prompt and reliable interventions.

Dynamic parameters of a structure such as modal frequencies, damping ratios, and mode shapes are known to be sensitive to changes in mass and stiffness, which may be related to damage [22]. These parameters can be obtained from vibration signals recorded via sensors during dynamic testing. This approach has recently been employed on various masonry structures such as towers [23–27], bridges [4,28–31], architectural heritage [32–34] and buildings [35–37] recently. However, the mentioned studies primarily focus on the entire structure, and the effects of damage on masonry walls' dynamic parameters have been rarely addressed or quantified. Masonry walls are the most common structural component for masonry structures and understanding this phenomenon can significantly benefit the monitoring of large-scale structures. Using a

straightforward but effective modal-based parameter to identify the overall strength reduction of monitored structures can be highly beneficial in the goal of developing simple techniques to assess structural state and strength. In this regard, the following questions are raised: *What are the dynamic characteristics of the masonry walls, and how do they change with damage*? *Does this change provide quantitative information on the damage that occurred*?

The current study addresses these questions by presenting experimental and numerical investigations. The experimental study focuses on the dynamic identification of damaged and undamaged masonry wall panels, considering the bare and strengthened conditions of the walls. As such, it enables observing the effects of the strengthening approaches and severe damage on the dynamic properties of the walls. Throughout this study, three stone masonry wall panels subjected to cyclic in-plane shear compression loads were tested. The first wall panel, denoted as the benchmark wall, was built with ashlar stones and natural hydraulic lime (NHL) mortar. In the construction of the second wall panel, a different type of mortar, fibre-reinforced mortar (FRM) with higher tensile strength was used. The third wall panel was constructed with NHL mortar, similar to the benchmark panel, and surface strengthening with textile-reinforced mortar was applied. Two types of excitations, ambient and impact, were utilized for dynamic identification and the vibration measurements were taken before and after the in-plane shear-compression tests. Then, the data obtained through acceleration sensors were used to find the natural frequencies, damping ratios, and mode shapes of the wall panels.

Moreover, special attention is given to tracing the damage progression and its effect on the dynamic features of URM wall panels. In order to complement the experimental investigations, the dynamic characteristics of the benchmark URM wall are further investigated via computational modeling using the discrete element method (DEM). The proposed numerical modelling strategy adopts a contact constitutive law which couples tension-shear and compression-shear damages together with stiffness degradation in the unloading-reloading regimes. The proposed DEM-based approach is validated via shear-compression test results and used to track the modal frequency change at intermediate stages of the damage. This way, the capabilities of the numerical approach in addressing the modal features are also investigated. In essence, this study enhances the existing collective understanding concerning the dynamic features of masonry walls. It achieves this by encompassing both intact and damaged states of the walls and by providing a quantitative assessment of the inflicted damage as well as the alterations observed in their dynamic attributes.

In addition, the improvement in the dynamic properties of the masonry wall panels upon using two strengthening approaches applied, with either fiber reinforced repair mortar or glass fiber mesh with FRM, is also presented. Such contributions will provide a step towards a better understanding of the dynamic characteristics of URM walls and help post-earthquake assessments of masonry structures.

2 Experiments

2.1 Masonry Wall Panels

Three wall specimens of 1.55 × 1.60 × 0.30 m^3 dimensions were constructed using machine sawn and smooth ashlar stones and two types of mortar. The stones are classified as "clayey-limestone," which has a composition of approximately 85% limestone and 15% clay. In addition to the stone blocks, NHL mortar, glass-fiber mesh, and FRM are the materials used in the construction of the specimens. The NHL mortar was prepared by mixing Teknorep 500 product and natural sand in 1:3 weight proportions. The amount of water was determined on-site as per the consistency requirements for ease of construction. Teknorep 500 is a commercially available natural hydraulic lime mix developed for applications in historical structures, and it contains no cement. The FRM mortar was prepared by mixing the Mape-Antique Strutturale NHL with water in 25:4 proportions (4 lt of water for a 25 kg bag). Mape-Antique Strutturale NHL is a pre-blended cement-free mortar in powder form for render and masonry work, made from natural hydraulic lime, Eco-Pozzolan, natural sand, special admixtures, micro-fibers, and glass fibers.

The mechanical properties of the masonry units (stone blocks) and mortar, which were determined from uniaxial loading tests, are as follows: the average compressive strength of stone blocks is 23.3 MPa, whereas the flexural-tensile strength is 4.45 MPa. The average flexural-tensile strength of NHL mortar is determined as 1.00 MPa, while the average compressive strength is 2.74 MPa. Further, the flexural-tensile and compressive strength of FRM mortar specimens are 3.69 MPa and 14.85 MPa, respectively. Finally, the average compressive strength of the masonry composite constructed using the NHL mortar is 12.3 MPa, obtained from the compression tests of masonry wallettes. Interested readers are referred to another study [38] comprising an extensive experimental campaign for further details.

The first wall panel is a benchmark specimen, and it was built with natural hydraulic lime mortar and ashlar stones. The second wall was constructed with FRM mortar, which has much

higher tensile strength compared to the NHL mortar. The effect of increasing the mortar's tensile strength on the stiffness and capacity of the wall is investigated. The third wall panel specimen was constructed with NHL mortar similar to the benchmark model, but its faces were strengthened with a glass-fiber mesh to investigate the effect of the strengthening in the wall's lateral load-carrying and displacement capacity. In the strengthening, Mapenet EM30 brand glass-fiber mesh (FRP) with $30mm\ x\ 30mm$ spacing was attached to the wall surface using the FRM mortar and connectors. In order to connect the wall specimens to the ground and move them in the laboratory, the walls were constructed on readily available reinforced concrete (RC) foundations that were attached to the strong floor during the tests. All wall panels were constructed on a 10 mm layer of high strength mortar of type BASF MasterEmaco S488, and the same was applied at the top of the wall to provide uniformity beneath the loading beam. All the specimens were cured for at least 28 days before the cyclic tests. Figure 1 displays the first and third wall panels during the construction.



(a) **(b)** **(c)**

Figure 1. Construction of the (a) first, (b-c) third wall panel.

2.2 Cyclic Shear-Compression Tests

In-plane cyclic shear-compression testing of the URM wall panels was carried out using a displacement-controlled lateral loading scheme described in ASTM-E2126-Standard Test Methods for Cyclic Load Test, Test Method B [39]. This loading scheme consists of two displacement patterns: the first one includes five fully reversed cycles at displacements of low

amplitudes (1.25% to 10% of the ultimate displacement) and the second one consists of three fully reversed cycles of equal amplitude starting from 20% ultimate displacement and increasing by 20% increments until failure. In the related document, the ultimate displacement refers to the one obtained from test under monotonic loading. However, in the absence of such a test, the ultimate displacement for the benchmark wall corresponded to 1.2% drift, and this value was used as the ultimate displacement in determining the loading cycles of the other two experiments. During the experiment, the vertical loading was kept constant at 230 kN, corresponding to 0.5 MPa average compressive stress, and controlled using the vertical loading jack and the load cell. In-plane angular deformations and vertical displacements on top of the wall during the test were not restrained. The out-of-plane movement of the wall was prevented at the top using two roller supports on both sides of the walls, allowing the in-plane movement of the RC loading beam at the top. Strain gauges and potentiometers were installed on both sides of the walls to measure the strains and displacements. Figure 2 illustrates the experimental setup used in the tests, also detailed in [40,41].

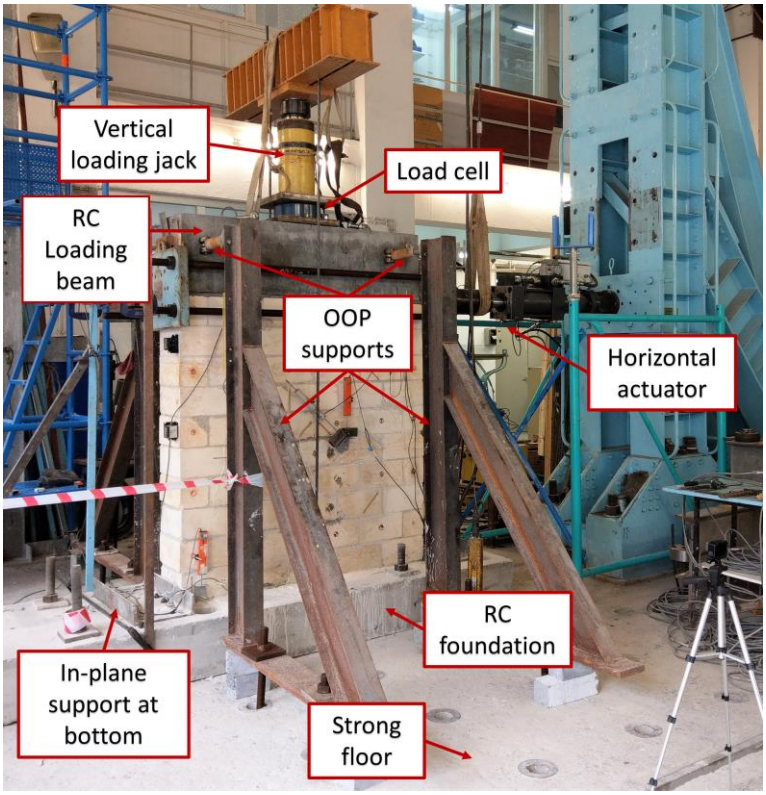

Figure 2. Experimental test setup.

It is worth noting that only the related details and results of the in-plane cyclic test of masonry panels are presented within the scope of this paper. The status of the walls after the cyclic tests and the force-displacement hysteresis curves are presented in Figure 3 and Figure 4, respectively, to give the reader a chance to correlate the system identification results with the type and amount of damage that occurred. A progressive damage mechanism, starting with flexural behavior, was noted in the benchmark wall panel, followed by a stepped-crack propagating from the right top to the left bottom corner at the stone-mortar interfaces at first; see Figure 3(a). Afterward, the compressive stresses at the lower course of the wall increased, and eventually, a crushing failure was observed. The third wall panel (Figure 3(c)) showed very similar mechanisms to the benchmark wall but had a much higher displacement capacity due to the presence of the glass-fiber mesh. The ultimate failure was reached upon the failure of the mesh reinforcement, as observed in similar studies [42]. Several stones of the glass-fiber mesh-strengthened wall, which were confined by the mesh, were pulverized. Both the benchmark wall and the glass-fiber mesh strengthened wall showed significant strength and stiffness degradation in their last cycles upon failure, which can be noticed in Figure 4(a) and Figure 4(c), respectively. Finally, the second wall, which was constructed using a mortar with a higher tensile strength, exhibited a monolithic behavior, and it rocked back and forth, crushing only the stones at the toe and heel. No significant strength and stiffness degradation was observed. The test was finalized due to the equipment reaching its displacement capacity. The reason for this behavior was the different chemical composition and high bonding strength of the FRM to the substrate. As such, different types of damage were observed for the three walls as shown in Figure 3.



(a) (b) (c)

Figure 3. Status of the (a) benchmark wall, (b) the second wall and (c) the third wall after the cyclic tests.

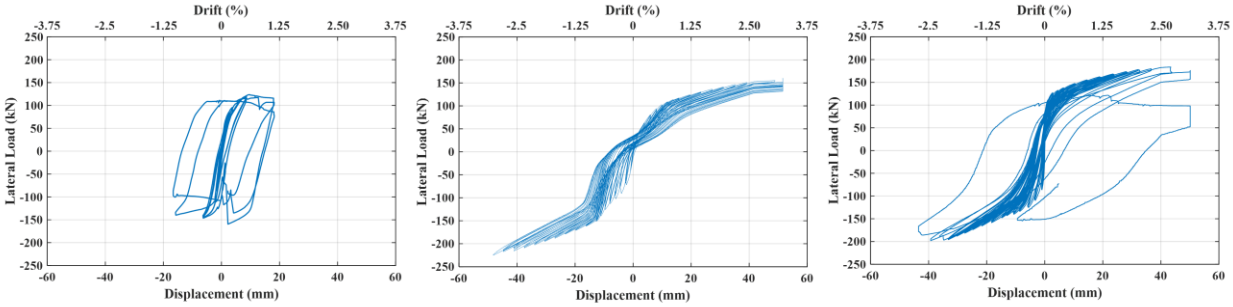

Figure 4. Hysteresis curves for (a) the benchmark URM wall, (b) the second wall with FRM mortar, and (c) the third wall with surface strengthening.

2.3 Dynamic Identification

2.3.1 Instrumentation and Tests

Vibration measurements were conducted on the walls with the test setup, i.e., considering its additional mass. Acceleration measurements under ambient vibrations and random impacts on the walls were taken using a 24-bit Kinemetrics Basalt recorder and five Kinemetrics Episensor ES-U2 type uniaxial force-balance accelerometers (FBA sensors), four of which are in out-of-plane directions, and the last one is in-plane, see Figure 5. Sensor properties include a user-selectable full g-scale range: from ± 0.25g to ± 4g and very-low self-noise provided as 155 dB dynamic range by the producer. Dynamic range is often characterized by the ratio between the full-scale output of a device and the noise products when the device is producing very low-level signals. The self-

noise of the sensors could significantly affect the quality of gathered data where vibration response levels are very low, such as under ambient vibrations. Therefore, it can be stated that the sensors used in this study are very suitable for ambient vibrations and provide better quality data. Approximately 60 minutes of data in each setup of ambient vibration tests and 15 minutes of data with random impacts were taken with a sampling frequency of 200 Hz. Ambient vibration and random impact tests were conducted before and after the cyclic tests were completed, which required disconnecting the actuator. Recorded data, an example is shown in Figure 6, were utilized to find the dynamic properties of the panel walls in their intact and damaged states. Note that ambient and impact vibration tests were conducted subsequently in a controlled laboratory environment; thus, variation in the environmental conditions is not a concern.

It should be stated that the location and number of instruments were determined based on identifying the first three modal frequencies and mode shapes only, and not with the purpose of rigorous damage detection. The approach used here is analogous to a typical real-world application where a limited number of sensors are placed sparsely on a structure in separate experimental campaigns, and the data is available only before and after the damage, such caused by an earthquake for example.

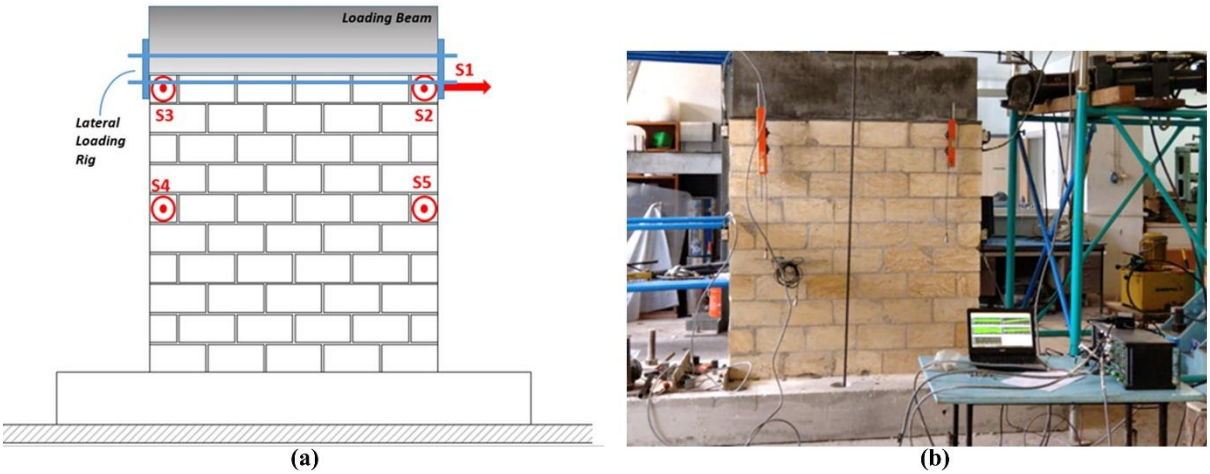

Figure 5. **(a)** instrumentation for dynamic identification tests and **(b)** test setup.

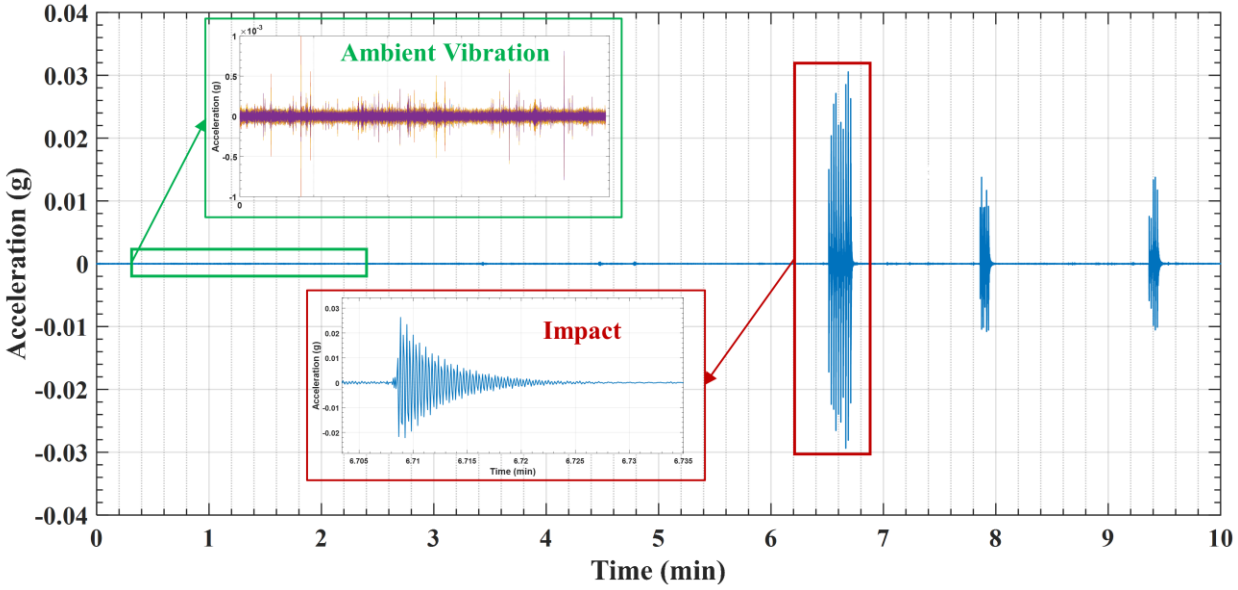

Figure 6. Acceleration data under ambient and impact vibrations.

2.3.2 Operational Modal Analysis

Frequency Domain Decomposition (FDD) [43] is a non-parametric output-only modal identification technique that operates in the frequency domain and has the advantage of being fast and user-friendly. The identification algorithm is implemented first by estimating the Power Spectral Density (PSD) matrix. In this study, the PSD matrix was determined using a MATLAB code that uses the Welch method, Fast Fourier Transform with 4096 points, a Hanning window, and an overlapping of 50%. Then, the estimate of the output PSD, G_{yy}, is decomposed by taking the singular value decomposition (SVD) of the PSD matrix.

$$G_{yy}(\omega_j) = U_j S_j U_j^H \quad (1)$$

where U_j is an orthonormal matrix ($U_j U_j^H = I$) that contains the singular vectors of $G_{yy}(\omega_j)$ and S_j is a diagonal matrix with the scalar singular values. As the spectral matrix is decomposed into a set of auto spectral density functions, each of these corresponds to an equivalent single degree of freedom system. By plotting the first singular values for each frequency, one can obtain the system's modal frequencies via simple peak-picking and the mode shapes using the first singular vectors at the corresponding frequency.

As an enhancement to the FDD technique, Enhanced Frequency Domain Decomposition (EFDD) [44] allows the identification of damping ratios. In order to determine a specific damping ratio, the PSD function around the peak is identified by comparing the mode shape estimate (the singular vector) at the peak with the singular vectors for the frequencies around it. This comparison can be made using the modal assurance criterion (MAC), which measures the correlation between two modal vectors [45]. The MAC value ranges between zero and one. If the singular vector and the mode shape vector have a high MAC value, the corresponding singular value belongs to the single degree of freedom (SDOF) density function. On the other hand, if the MAC value drops below the user-defined threshold for a specific frequency, then the search for matching parts of the auto spectral density function is stopped, and the rest of the values (the remaining portion of the function) is set to zero. Afterward, we use the inverse fast Fourier transform to take the spectral density function back to the time domain to find the natural frequency and damping ratio. Since the impulse response of a dynamic system and the system's output correlation when excited by a white noise are proportional, the modal damping ratio of the mode under investigation can be estimated by the logarithmic decrement of the free decaying autocorrelation function of the SDOF system. Also, an improved estimate of the natural frequency can be done from the crossing times of the function. Magalhães and Cunha [46] describe the method in detail and present informative illustrations. Examples of the damping identification from the impulse response function can be seen in Figure 7 and the power spectra of the records are given in Figure 8. Identified modal parameters are presented in the next section of the paper.

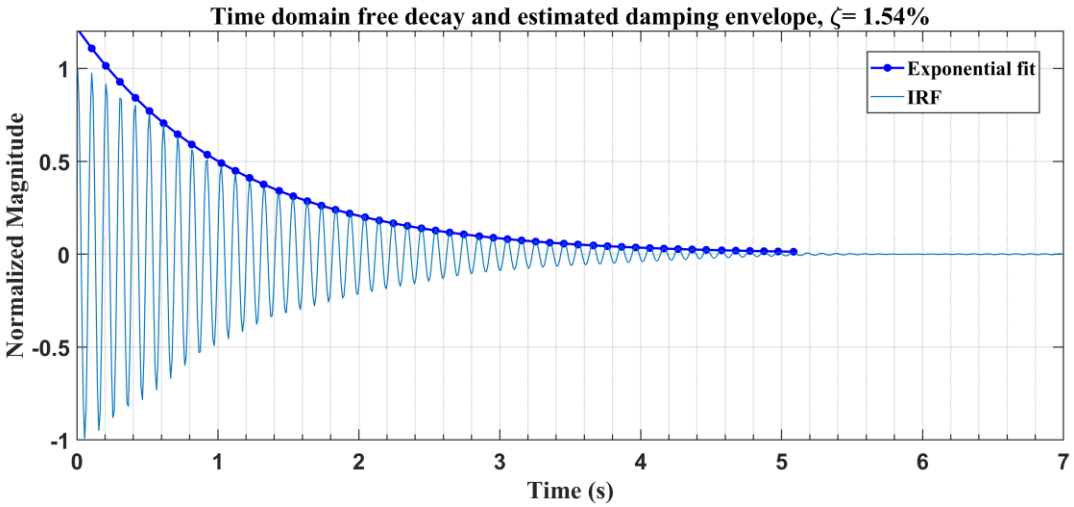

Figure 7. Example of the impulse response function and damping envelope for damping identification.

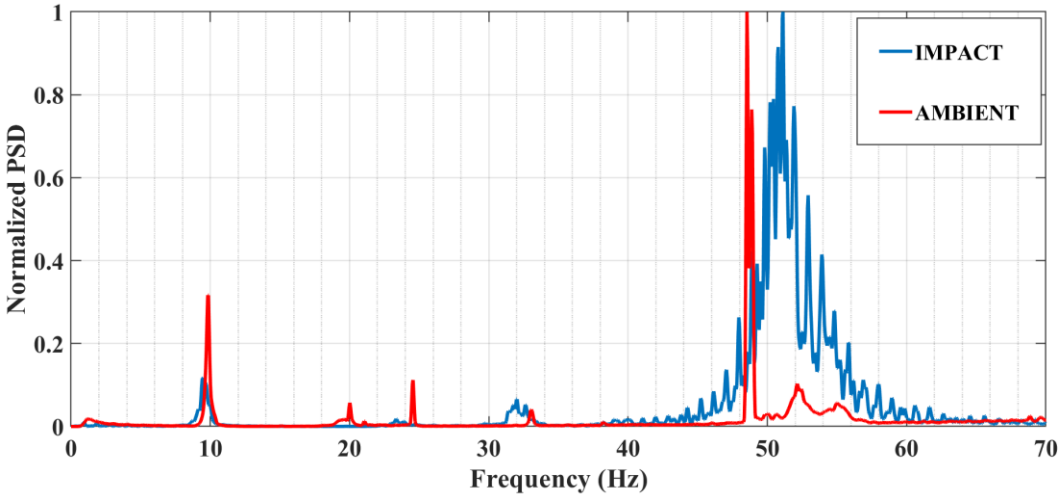

Figure 8. Comparison of normalized power spectra for ambient vibration and impact data for the first wall before the cyclic test.

From Figure 8, it is possible to notice that the power spectra obtained after processing the data are slightly different depending on the type of excitation, *i.e.*, ambient vibration or impact. Therefore, the structure's dynamic properties identified using system identification also slightly vary depending on the type of excitation used. The fundamental frequencies obtained from impact excitation data are up to 8% lower than their counterparts identified from ambient vibration data. This difference is because the impact vibration magnitudes are very high compared to those from

ambient vibrations, reaching magnitudes 500 times higher, resulting in higher damping in masonry. As the amplitude of the excitation increases, the damping also increases. For ambient vibrations the damping ratio is small (less than 3%), and the damping ratios obtained from the time-history of raw data, using the decline of impact vibrations and logarithmic decrement approach, are in the similar range with the values obtained from EFDD identification; therefore, the two different approaches confirm the results of each other. On the other hand, it is known that the damped natural frequency of the system is lower than the undamped natural frequency as per the equation $f_d = f_n\sqrt{1-\zeta^2}$, where f_d and f_n are the damped and undamped natural frequencies, respectively, and ζ is the damping ratio. If the reason for the decline in the identified frequencies were purely damping, then such a decrease would require the damping ratio to be 20-30%, which is significantly high when there is no observable damage. We think that the decrease in the frequencies can also be related to other factors, such as the time-dependent and amplitude-dependent behavior of the masonry material. Because the natural frequency of a single degree of freedom system is a direct consequence of its stiffness, and we typically determine the stiffness as a ratio of force and displacement ($k = f/d$), analyzing the effect of the force amplitude on the definition of the stiffness might help. Masonry is a highly nonlinear material and it is possible that the effects of ambient vibrations on the structure remain in the elastic range of the material's force-displacement behavior corresponding to the initial stiffness of the wall. On the other hand, the amplitude of excitations under impact vibration is much higher and these actions correspond to points in the force-displacement curve with a lower stiffness, determined by the secant stiffness. Another factor for the decrease in the identified frequencies can be that the uncertainty in the identified parameters is larger for impact vibrations as the amount of data is much smaller compared to the ambient vibrations. Considering these factors for the effects of impact vibrations on the dynamic identification results, it may not be accurate to obtain dynamic properties from the impact vibrations, especially for damaged masonry walls. During testing, vibrations caused by several pieces of laboratory equipment were also measured by acceleration sensors. Those types of equipment have specific working (or forcing) frequencies. They are called *harmonic* frequencies, and spurious peaks that belong to those frequencies are also represented in the power spectra depending on their energy content. When placed in the vicinity of the fundamental frequencies, the so-called harmonic frequencies can represent the individual mode shapes or a mixture of them. Therefore, they are often confused with fundamental frequencies of the structure

during system identification. In that sense, the effect of the impacts might amplify the harmonic frequencies in the PSD graph and cause overlooking of the structural frequencies, which was the case for the benchmark wall. This phenomenon is clearly observed in Figure 8, where the normalized PSD of the impact and ambient vibration data for the first wall before the cyclic test is compared. A harmonic frequency stemming from the electrical equipment, around 50 Hz, is mixed with the third modal frequency when the impact excitation is imposed. In addition, the magnitude of the peak corresponding to the harmonic frequency causes other much smaller structural peaks to be missed, such as the second mode frequency, which is around 20 Hz. This deficiency originates from the short vibration record of impact excitation compared to the ambient vibration record. Moreover, the contamination of the power spectrum of the impact vibrations is likely to lead to inaccurate modal parameter estimation. Thus, we decided to use ambient vibrations for modal parameter identification in this study and provided the counterparts obtained from impact vibrations where necessary.

2.3.3 Results and Discussions

A summary of the modal frequencies obtained from ambient vibration and impact records are presented in Table 1. The increase in the structural frequencies for the second and third wall-panels demonstrates that the walls' behavior has changed compared to the first wall, since the stiffness has increased and that the strengthening effects are observable. The first three mode shapes of the intact benchmark wall that are also representative of the strengthened walls are illustrated in Figure 9. The identified mode shape vectors before conducting the cyclic tests are also presented in Table 2. The first mode of the wall-panels correspond to the out-of-plane bending of the wall with single curvature (see also Figure 15(a)), the second mode is the in-plane shear behavior of the wall (Figure 15(c)), and the third mode corresponds to the second out-of-plane bending mode with single curvature and sides of the wall are out-of-phase, which could also be characterized as the torsional behavior (Figure 15(b)). Therefore, we will call the first three modes bending, shear and torsion modes, respectively, throughout the text for brevity.

Table 1. Summary of the modal frequencies.

	Ambient-Vibration (Hz)			Impact-Vibration (Hz)		
	f_1 (bending)	f_2 (shear)	f_3 (torsion)	f_1 (bending)	f_2 (shear)	f_3 (torsion)
Wall 1	9.86	21.05	48.53	9.42	32.03	51.12
Wall 1-after test	8.11	17.63	24.61	7.81	17.43	24.16
Wall 2	14.16	23.00	48.88	12.99	22.85	47.85
Wall 2-after test	8.98	17.14	40.28	8.30	16.85	38.28
Wall 3	14.69	23.82	52.30	13.96	28.52	51.02
Wall3-after test	8.50	18.55	29.30	8.15	18.25	28.22

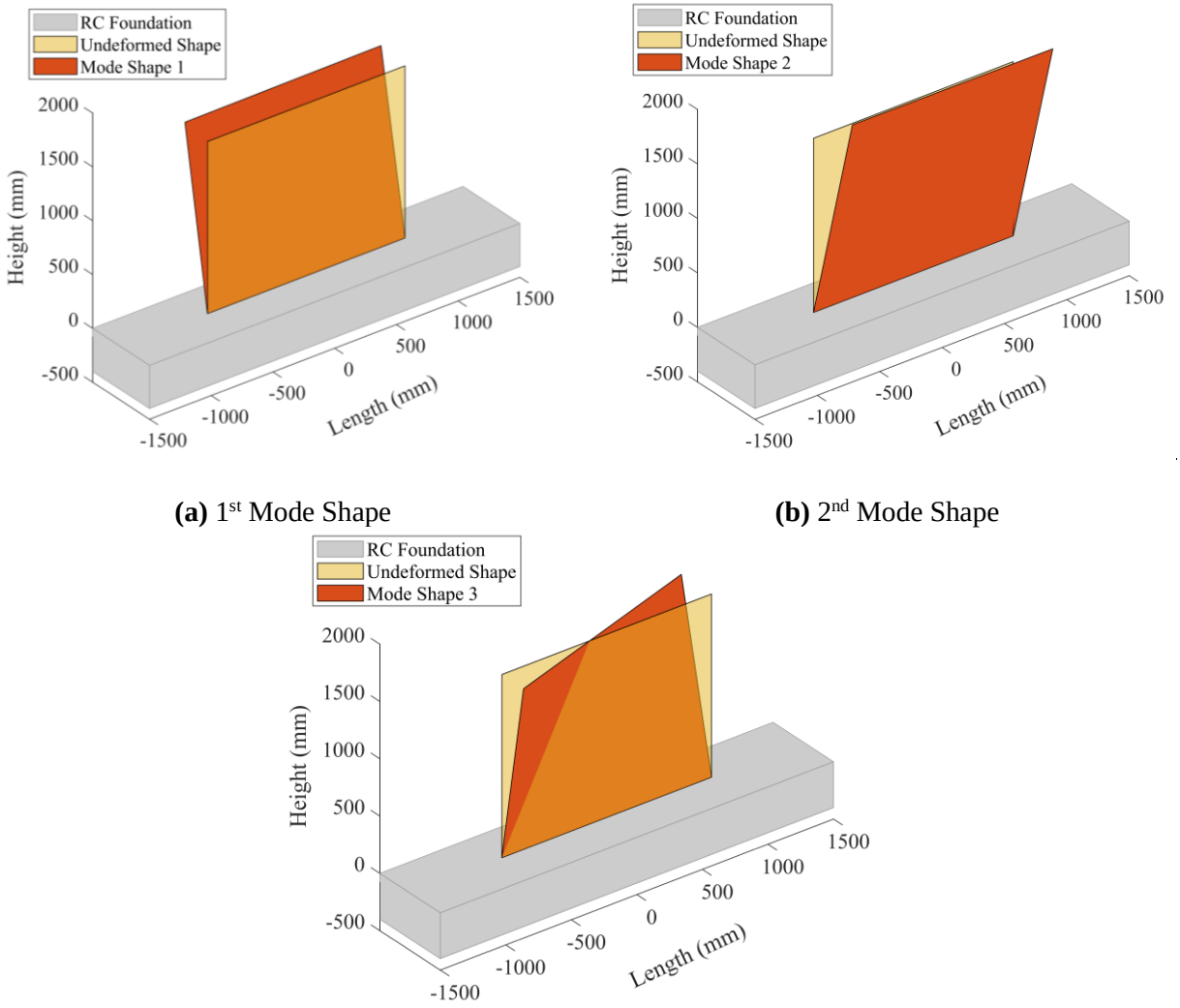

(a) 1st Mode Shape **(b)** 2nd Mode Shape

(c) 3rd Mode Shape

Figure 9. First three identified mode shapes of the intact benchmark wall.

Table 2. Summary of the normalized mode shape vectors before cyclic tests.

	Normalized Mode Shape (MS) Vectors								
	Wall 1			Wall 2			Wall 3		
Sensors	**MS1**	**MS2**	**MS3**	**MS1**	**MS2**	**MS3**	**MS1**	**MS2**	**MS3**
S1	0.12	1.00	0.00	0.08	1.00	0.03	0.08	1.00	0.03
S2	1.00	-0.08	1.00	1.00	0.00	1.00	0.99	0.25	0.93
S3	0.95	-0.05	-0.72	0.88	0.12	-0.95	1.00	0.32	-1.00
S4	0.53	0.00	-0.42	0.56	0.08	-0.70	0.60	0.19	-0.71
S5	0.56	0.01	0.48	0.66	0.00	0.76	0.62	0.11	0.70

The apparent decrease of the fundamental frequencies after the cyclic tests due to damage, presented in Table 3, indicates that the occurrence of damage can be successfully detected. However, it is difficult to estimate the decrease in structural frequencies due to damage as the amount of damage and decrease in the structural frequencies are different for the types of damage observed. For the benchmark and third walls, where the damage mechanisms are similar, the decrease in the frequencies of the out-of-plane modes is much higher compared to the decrease in the in-plane mode frequency. This observation is also intuitive as the out-of-plane resistance of these two damaged walls is minimal and stems only from self-weight. As the out-of-plane force-displacement data during the test is not available, the amount of damage corresponding to the out-of-plane behavior, *i.e.*, the reduction in the bending stiffness of the walls could not be quantified.

Table 3. Decrease in the structural frequencies after the cyclic tests.

	Ambient-Vibration Data			Impact-Vibration Data		
	Decrease in Modal Frequencies			Decrease in Modal Frequencies		
	f_1 (bending)	f_2 (shear)	f_3 (torsion)	f_1 (bending)	f_2 (shear)	f_3 (torsion)
Wall 1	17.7%	16.2%	49.3%	17.1%	45.6%	52.7%
Wall 2	36.6%	25.5%	17.6%	36.1%	26.3%	20.0%
Wall 3	42.1%	22.1%	44.0%	41.6%	36.0%	44.7%

The in-plane stiffnesses of the walls decreases significantly upon failure. As we have the whole in-plane cyclic behavior, we can extract the reduction in the in-plane stiffness by comparing its value at the beginning and end of the entire loading. The initial and final in-plane lateral stiffnesses of the first wall are calculated using the hysteresis force-displacement curves given in Figure 10, as 63.2 kN/mm and 12.24 kN/mm, respectively. The unloading secant stiffness [47], which is the slope of the curve passing through two points*: i)* the point of maximum displacement of the

corresponding load cycle and the load at this point, and *ii)* the point of zero force with the corresponding initial displacement at the same loading cycle, is used to calculate the stiffness at the first and final cycles. Note that the last cycle corresponds to the third cycle to the ultimate displacement. Therefore, there is 80.6% reduction in the in-plane stiffness whereas the reduction in the in-plane shear mode (2nd mode) frequency is determined in the range of 16-45% (depending on the ambient or impact vibrations). Therefore, it can be stated that the amount of the change in the frequencies after the tests can be tracked, but in order to infer it directly from the observed damage more experiments covering intermediate stages of damage and various excitation types are necessary.

In addition, it was discerned that after the damage, detecting the second and the third mode shapes becomes more difficult. In the damaged state, the stones are still in contact despite the existence of large cracks, but separate macro blocks may occur and form local modes of vibration with different characteristics than the global modes. Considering this added complexity, the higher (2nd and 3rd) modes were more difficult to discern, and some presented significant differences to the ones obtained in healthy states, and these mode shapes were even coupled in some cases. We focused only on the global modes in this study; however, local differences in the identified mode shapes are often associated with the formation of local vibration modes in the literature, and it should be highlighted that the continuity of the masonry structures after damage and its effects on the behavior deserves more research.

At this point, it should be stated that the dynamic behavior of the wall panels depends on multiple modes and various stiffness components, such as bending, shear, sliding etc. If a more detailed approach is used such as measuring the dynamic properties of the walls at each cycle of loading, some of the simple mechanisms of wall failure like rocking, sliding or diagonal tension, and their strength degradation might be parametrically related to the dynamic properties of the walls. Indeed, such an approach is demonstrated by Giordano et al. [47] as an excellent example of such methodology, where they tested simple adobe arches and correlated the progressive damage to the frequency shift in one of the observed structural modes. Such a study for masonry walls would require a significant number of experimental tests, dismantling the actuator and test setup at every cycle, for a specific pure failure mode (like bed-joint sliding) to be described analytically. More recently, the same approach was applied to the in-plane cyclic shear testing of an adobe wall by the same research group [48]. Their study also suffered from the previously

mentioned difficulties, like the number of specimens and feasibility of intermittent measurements, etc., and no descriptive relationship between the frequency decrease and damage could be found.

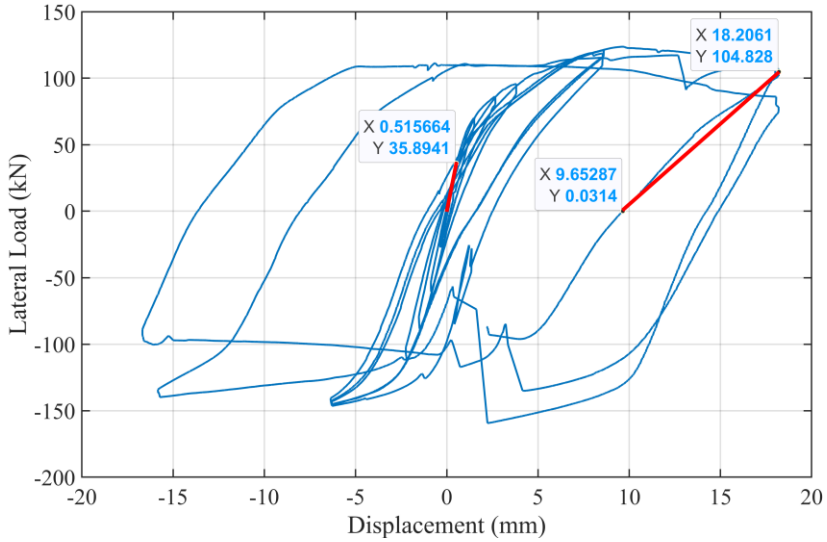

Figure 10. Hysteresis curves used to calculate the initial and final lateral stiffness of the first wall.

The summary of the modal damping ratios estimated using the ambient vibration data is presented in Table 4, with the values corresponding to tested walls designated as damaged. No significant increase in the damping ratios was observed even though the wall panels were tested up to failure. This stems mainly from the use of ambient vibrations whose vibration amplitudes are very low, and the closing of existing cracks with the self-weight and additional weight of the equipment on top of the wall. In addition to the uncertainties and issues related to damping ratio estimation in the frequency domain [28], the presence of the noise and its adverse effects on the shape of the IRF were predominant, especially for higher modes with high frequencies. This made the damping ratio estimation more cumbersome, except for the first mode. The experimentally determined modal damping ratios are in the range of those for existing masonry structures; however, the uncertainties and difficulties in the damping ratio estimation for higher modes should be accounted for in this study. It is also appropriate to state that the damping is amplitude-dependent, and the damping ratios increase with higher amplitude excitations.

Table 4. Summary of the modal damping ratios.

	Modal Damping Ratio (%)		
	ξ_1	ξ_2	ξ_3
Wall 1	1.54	0.30	0.46
Wall 1/damaged	1.77	0.37	0.69
Wall 2	2.01	1.02	0.99
Wall 2/damaged	1.74	1.68	0.83
Wall 3	1.17	1.13	1.09
Wall3/damaged	2.69	1.17	1.69

3 Discontinuum-Based Analysis and Modal Identification of Benchmark Wall

This section investigates the in-plane behavior of the benchmark URM wall together with the modal frequency and mode shapes using the simplified micro-modeling approach within the discrete element method (DEM) framework. First, the computational procedure of the adopted modeling strategy is explained. Then, verification of the numerical model is performed by simulating the force-displacement behavior of the benchmark wall and the observed damage under quasi-static loading. This numerical model is further utilized to investigate dynamic properties of the wall and how they change with the damage occurred. Thus, the results of the validated discontinuum-based analysis are presented, and modal properties are compared with the experimental findings.

3.1 Computational Procedure of the Discrete Element Method

Computational modeling of unreinforced masonry structures can be grouped into continuum and discontinuum-based analyses. The former approach considers the composite structure of masonry as a continuous medium with no distinction between the masonry unit, mortar, and unit-mortar interface, while the latter considers the constituents of a masonry wall explicitly. Throughout this research, the DEM, falling into the category of discontinuum-based analysis, is used to perform quasi-static and modal analyses of the benchmark wall. Specifically, the masonry units are simulated via distinct rigid blocks interacting along their boundaries, and unit-mortar interfaces are represented through zero-thickness interfaces, as illustrated in Figure 11. Note that two blocks are utilized to simulate each masonry unit considering a potential crack surface (Figure 11(a)). Furthermore, the mechanical interaction among the adjacent blocks is computed at the

contact points (also denoted as sub-contact) defined at the center and mid-length of the contact surfaces (see Figure 11(b)).

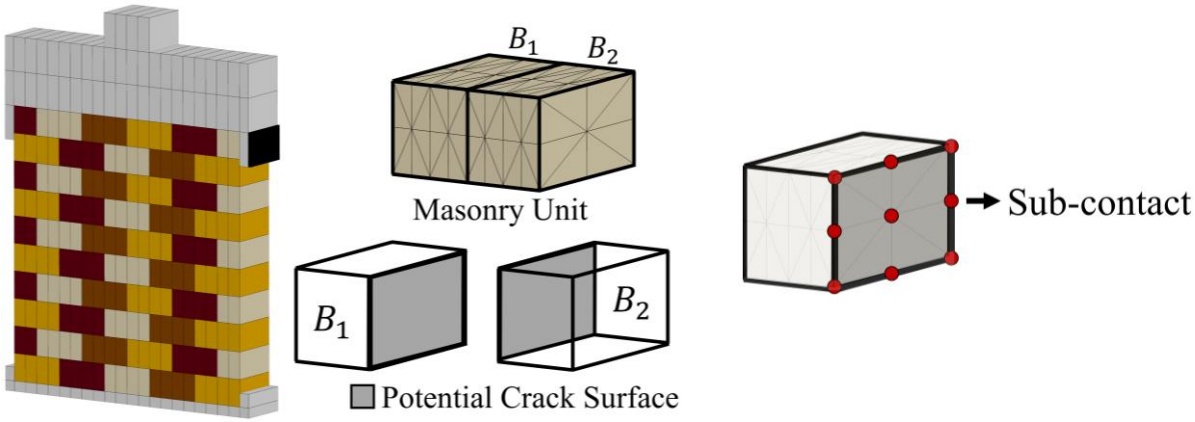

Figure 11. (a) Discrete element model and (b) illustration of sub-contact.

The computational procedure of DEM relies on integrating translational and rotational equations of motion for each rigid block in the system. The governing differential equations are solved via the central difference method to predict the new velocities, which are later multiplied by the time step to obtain the displacement of the blocks. According to the updated position of the blocks, relative sub-contact displacement in the normal (u_n) and shear (u_s) directions are obtained that are further utilized to compute normal (σ) and shear (τ) contact stresses at the active contact points, respectively. At each contact point, three orthogonal springs are defined, one in the normal and two in the shear direction. The overlapping between the adjacent blocks is allowed in the adopted numerical formulation, which is associated with the defined normal (k_n) and shear (k_s) contact stiffness. Elastic response is controlled by the linear springs, and the post-peak regime is defined based on the mode-I (G_f^I), mode-II (G_f^{II}) and compressive (G_C) fracture energies for tension, shear, and compression, respectively, as shown in Figure 12a. The Mohr-Coulomb failure criterion is used for shear with tension- and compression cut-off, as illustrated in Figure 12b. Upon failure in the normal direction (either in tension or compression), secant stiffness is used for unloading and re-loading scenarios [49,50]. The shear strength is computed using bond cohesion (c) and friction angle (ϕ) parameters. Furthermore, the tension and compression capacity at the

contact points are limited by the bond tensile strength (f_T) and compression capacity of masonry composite (f_m). It is worth noting that the two-way coupling mechanism is implemented using a single damage parameter for tension-shear interaction, whereas one-way coupling is considered for compression-shear [51]. In other words, upon failure, either in tension or shear, both mechanisms are influenced by the damage. On the other hand, in compression-shear interaction, only compression failure reduces cohesion, while the shear mechanism does not affect compression strength. The readers are referred to the reference study for further details about the utilized contact constitutive models [51].

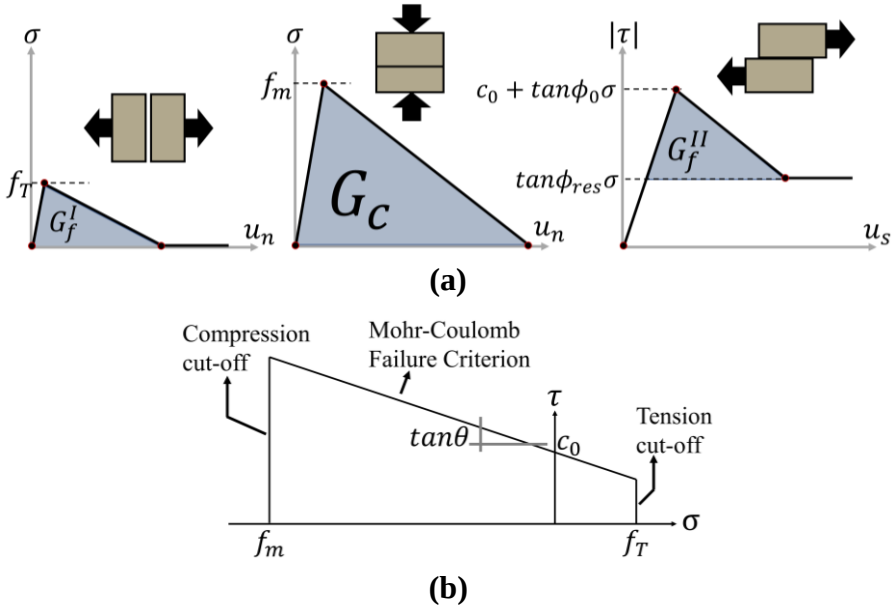

Figure 12. Implemented failure criterion (a) and the adopted contact stress-displacement laws in normal and shear directions (b).

Once the contact stresses are obtained, they are multiplied by the associated sub-contact area and utilized in the equations of motion to predict the translational and rotational velocities for the next time step. The quasi-static solutions are obtained via Cundall's local damping formulation [52], and numerical stability is ensured using a satisfactorily small time step (Δt), lower than the critical value ($\Delta t_c = 0.2\sqrt{m_{min}/k_{n,max}}$, m_{min}: minimum block mass and $k_{n,max}$: maximum contact stiffness in the system). Throughout this research, a commercial three-dimensional discrete element code, 3DEC developed by Itasca Consulting Group, is used [53], and the implemented

contact model is compiled as DLL (dynamic link library) into 3DEC via user-defined constitutive model option.

3.2 Verification of DEM Model

The adopted discontinuum-based modelling strategy is first validated by comparing it against the experimental results obtained from the cyclic testing of the benchmark URM wall. Two different loading scenarios are considered in the computational investigations: monotonic (also called pushover) and cyclic. The material properties are defined utilizing the available material characterization tests provided in [38], while the missing parameters are taken from similar studies published in the literature [40,41] and recommendations presented in [54]. The contact stiffness for unit-mortar interfaces is determined as $k_{n,j} = 13.31$ GPa/m for normal and $k_{s,j} = 5.31$ GPa/m for shear directions, respectively. These values were computed from: $k_{n,j} = E_{wall}/h$ and $k_{s,j} = 0.4k_{n,j}$, where h and E_{wall} are the average vertical spacing and macro-elastic modulus of URM wall, respectively. Material properties are summarized in Table 5.

Table 5. Contact properties defined for unit-unit (denoted via subscript u) and unit-mortar interface (denoted via subscript j) interactions.

Interaction within the stone masonry units			
$f_{T,u}\ (MPa)$	$c_{0,u}\ (MPa)$	$\phi_{0,u}\ (°)$	$\phi_{res,u}\ (°)$
1	2	40	40
$f_{c,u}\ (MPa)$	$G_f^I\ (N/m)$	$G_f^{II}\ (N/m)$	$G_c\ (N/m)$
23.3	30	550	23000
Interaction between the masonry units			
$f_{T,j}\ (MPa)$	$c_{0,j}\ (MPa)$	$\phi_{0,j}(°)$	$\phi_{res,j}\ (°)$
0.2	0.2	30	30
$f_m\ (MPa)$	$G_f^I\ (N/mm)$	$G_f^{II}\ (N/mm)$	$G_c\ (N/m)$
5.5	$0.015f_{t,j}$	$15G_f^I$	13200

The assigned boundary conditions and the loading setup are replicated from the benchmark study by considering cantilever behavior, *i.e.*, fixed at the bottom and no restriction on top along the in-plane direction, with a lateral point load prescribed for a rigid block attached to the loading beam. After the equilibrium condition is satisfied under the self-weight of the system, the pre-compression pressure (0.5 MPa) is applied to the loading beam. A total of 274 discrete blocks is

used in the discontinuum model with nearly 1000 contact points. The computational cost for the pushover analysis is noted as 25 minutes, using a computer system with AMD Ryzen 7 5700X desktop processor (8 CPU cores) and 16 GB memory RAM. The applied load and top displacement are monitored and recorded throughout pushover and cyclic analyses. The force-displacement curve obtained from pushover analysis and the associated collapse mechanism is shown in Figure 13(a) and Figure 13(b), respectively. Note that in Figure 13(a), the envelope force-deformation relationship obtained from the experiment is used for comparison. Overall, a good agreement is found between the experimental results and the discontinuum-based analysis. The progressive damage is noted as follows: the flexural cracks are initiated at the bottom right corner of the wall, and then the diagonal shear crack is developed toward the later stages of the analysis (around a top displacement of 8 mm). Finally, it turned into a predominantly sliding mechanism after 14 mm. It should be highlighted that the observations gathered from the numerical model align with the experimental findings.

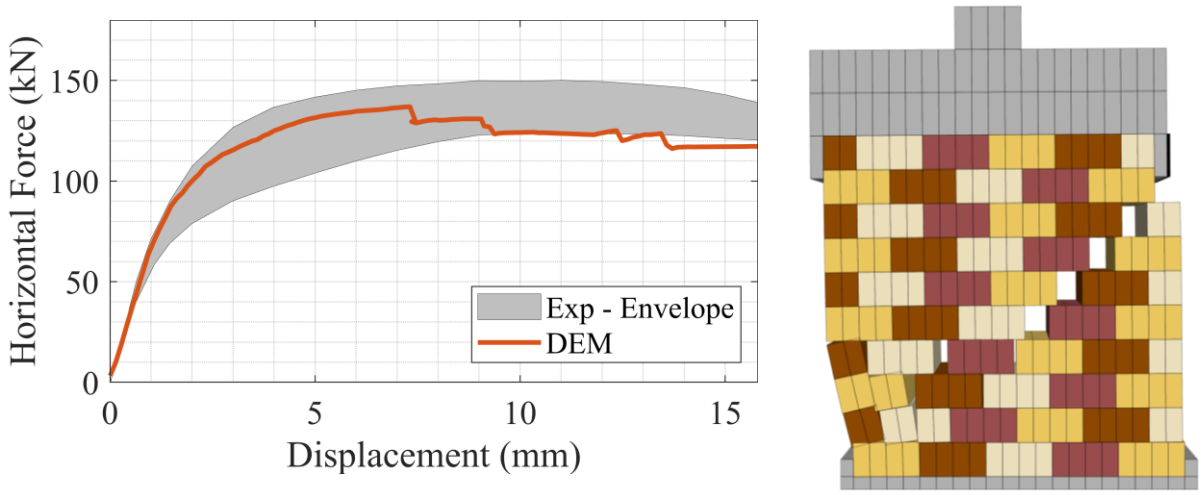

Figure 13. (a) Comparison of discontinuum-based analysis (DEM) and experimental results and (b) the collapse mechanism using monotonic loading.

Next, the same computational model is used to explore the cyclic behavior of the analyzed URM wall. A fairly good agreement is observed from the results of the analysis, as shown in Figure 14. In line with the pushover analysis, the initially started rocking mechanism evolved to the mixed diagonal tension and sliding failure at the joints, which caused significant stiffness and strength

degradation during the cyclic loading. It should be noted that the numerical model verification is carried out by accurately capturing the nonlinear quasi-static behavior of the benchmark wall, as this approach is a common practice in the literature. However, the objective here is not to validate the used DEM approach but to investigate the progressive change in the dynamic properties and the performance of the numerical model in estimating the dynamic properties of the damaged wall, which is presented in the next section.

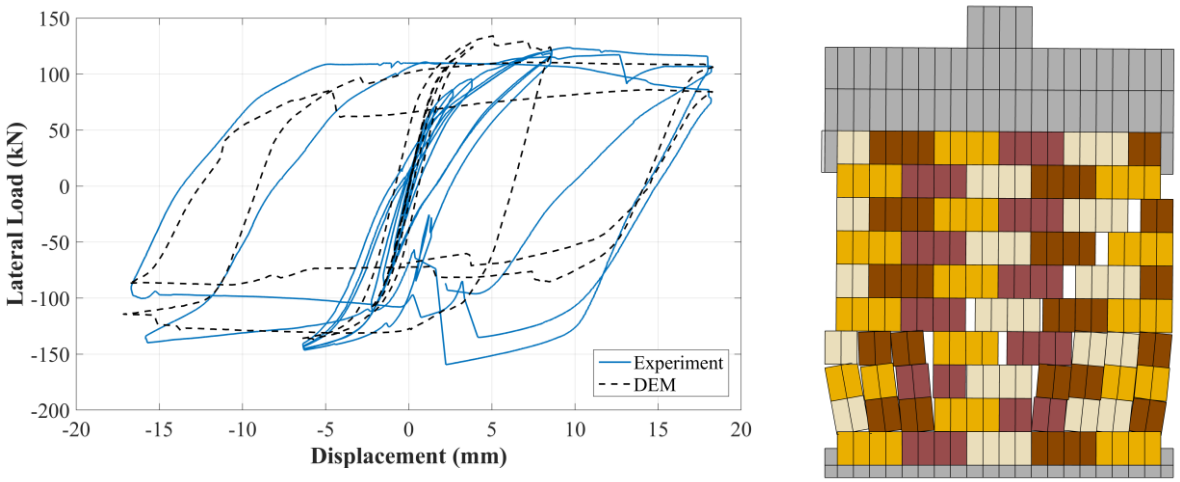

Figure 14. (a) Comparison of discontinuum-based analysis (DEM) and experimental results and (b) the collapse mechanism using cyclic loading.

3.3 Modal Analysis Before and After Damage

The validated numerical model is further utilized to explore the modal properties (*i.e.*, modal frequencies and mode shapes) of the benchmark wall. Since the proposed modelling strategy consists of rigid blocks only, the deformation is lumped at the joints, which is controlled by the contact stiffness. Before and at the end of the monotonic and cyclic loading tests, modal identification is performed by solving the eigenvalue problem in 3DEC, and the associated frequencies are given in Table 6. The results for the damaged case are extracted when the top displacement reaches 16 mm.

In the undamaged (healthy) state, the first mode shape indicates an out-of-plane bending behavior, while the second mode shape denotes torsion with sides of the wall out of phase, as illustrated in Figure 15. The third mode shape is an in-plane mode similar to the behavior under

shear effects. In the damaged state, the second and third modes change the order, such that the third mode becomes the second and vice versa; however, the shapes remain very similar. Comparing the modal frequencies before and after damage, the first two modal frequencies are the ones affected the most by the damage, and the mode shapes are similar to the experimental modes with slight differences, which are detailed in Section 2.3.

Table 6. Modal frequencies obtained from DEM analysis and experimental frequencies for the benchmark wall.

DEM Model		f_1	f_2	f_3
Before Analysis	No damage (Hz)	9.02	27.72	27.83
Monotonic	Damaged (Hz)	8.38	25.66	27.25
	Difference (%)	7.10	7.40	2.10
Cyclic	Damaged (Hz)	7.13	19.60	25.80
	Difference (%)	20.96	29.30	7.29
Experimental		f_1	f_2	f_3
	No damage (Hz)	9.86	21.05	48.53
	Damaged (Hz)	8.11	17.63	24.61

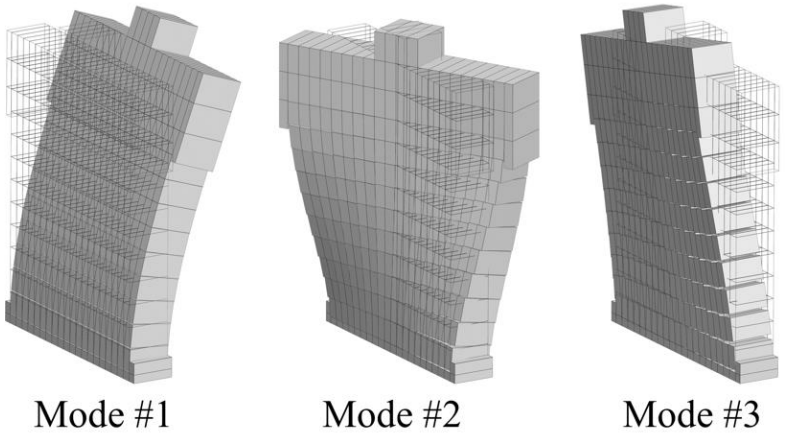

Figure 15. Modal shapes obtained from the computational model (before damage).

Next, the influence of damage on the first mode frequency is further investigated by carrying out modal analyses after reaching three intermediate damage states at lateral displacements of 4.8, 8 and 12 mm during the monotonic loading. The first modal analysis is carried out at the

undamaged state of the wall, whereas the second modal analysis is conducted once the wall shows significant nonlinearity at 4.8 mm. Still, the wall has not reached its capacity. For the third modal analysis, an intermediate stage of 8 mm lateral displacement approximately when a diagonal crack occurs is chosen. Then, the monotonic loading is also stopped at 12 mm, where a considerable drop in the lateral load carrying capacity occurs, and the eigenvalue problem is solved. Finally, the last modal analysis is carried out at the ultimate state of the wall at 16 mm displacement. The results highlight the strong relationship between damage accumulating around 4 mm and the decreasing trend of the first modal frequency, as shown in Figure 16. This figure displays, in a double y-axis plot, the monotonic force-displacement behavior of the benchmark wall and the evolution of the first modal frequency at different damage states, both obtained from the DEM analysis. In the same figure, we also present the first modal frequency obtained from the ambient and impact vibration tests at two instances: the healthy and collapse damage states, corresponding to zero- and 16-mm displacements in the figure, respectively. Once the modal frequencies obtained from DEM-based simulation and experiments using ambient and impact vibrations are compared, it is observed that the proposed computational model slightly underestimates the undamaged modal frequencies. This is expected as the static elasticity modulus of masonry is often lower than the dynamic elasticity modulus obtained via ambient vibration tests [55]. We also observe that the DEM model overestimates the first modal frequency of the damaged condition of the URM wall, as seen in Figure 16, when the loading is prescribed as monotonic. However, a lower first modal frequency is computed after the cyclic analysis, suggesting a widespread damage at the joints and masonry units as expected, see Figure 14.

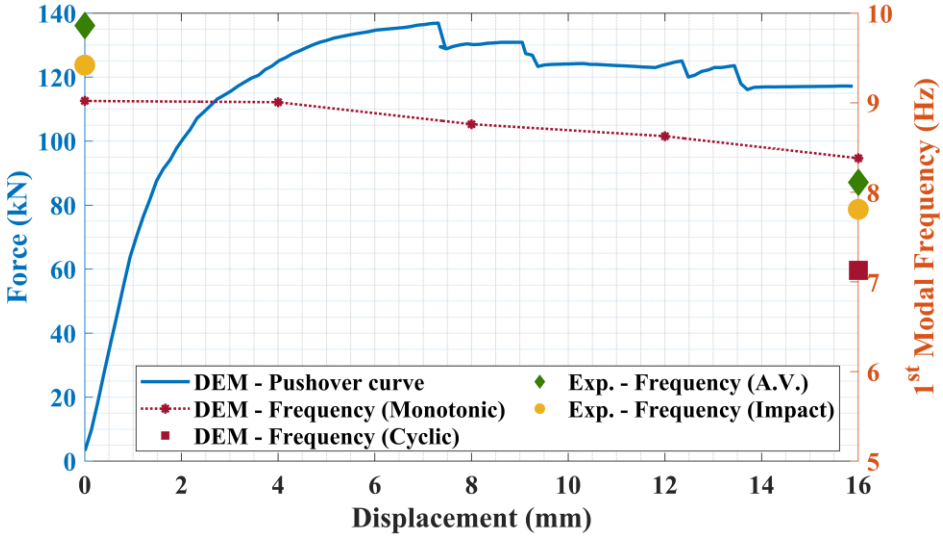

570 **Figure 16**. The first modal frequency from experimental identification and numerical analyses at different
571 levels of lateral displacement of the benchmark wall.

572

573 The comparison of the numerical modal analysis and experimental identification results in
574 Table 6 indicate that the modal properties of the numerical model deviate, especially for higher
575 modes, from the experimentally obtained ones even though the numerical model has been shown
576 to predict the force-displacement behavior and damage patterns accurately. Further, the changes
577 in the modal frequencies after the benchmark wall is tested to failure are observed to be
578 significantly different for the DEM analysis results when the monotonic loading is used. The main
579 reason for such discrepancy is the type of loading, which does not address the potential cyclic
580 degradation in the numerical model. On the other hand, a much better prediction is obtained from
581 the cyclic analysis that reasonably captures the stiffness degradation.

582 These observations motivate investigating the effects of the analysis type and nonlinear
583 parameters of the model, developing more advanced material models, and updating of discrete
584 element models before and after damage to enable more accurate predictions of the modal
585 properties once the damage occurs. This would also allow complementing the experimental work
586 with numerical models further and predicting the modal displacements of non-instrumented
587 portions of the structure, *i.e.*, increasing the spatial resolution of the information we have. It should
588 also be noted that model updating is commonly employed for structures behaving in their linear
589 range and might not be considered accurate for highly nonlinear structures such as masonry walls.

Therefore, there is a clear need for similar studies exploring the modal properties in the nonlinear range as well.

When the mode shapes obtained from the experiments and numerical analysis are investigated, it is possible to deduce another set of important conclusions. Primarily, the second (torsion) and third (shear) numerical mode shapes (Figure 15) are interchanged in the experimental results. This phenomenon demonstrates that the masonry is not isotropic, and the in-plane stiffness of this particular wall is much lower than the isotropic case, causing a significant drop in the modal frequency of the shear mode.

4 Conclusions

This study focused on the evaluation of modal properties of masonry wall panels in healthy and severely damaged states using ambient vibration and impact records, and advanced numerical analysis. Due to the resemblance of features such as limited number of sensors compared to the size of the structure and measurements at discrete times, *i.e.*, before and after damage, the presented study could be related to a real-life earthquake damage detection application. Albeit, the authors explicitly acknowledge that the limited number of sensors was not intended to simulate this condition. A benchmark unreinforced masonry wall constructed with NHL mortar and two other masonry walls, constructed with FRM mortar or strengthened with fibre mesh, were tested in in-plane cyclic shear-compression loading, and acceleration vibrations were measured before and after the tests. Dynamic properties of the wall panels were obtained by processing the data in the frequency domain. Then, a DEM-based micro-modeling approach was used to model the benchmark wall, investigate the change of modal properties at different levels of damage using a validated model. Experimental and numerical modal properties were compared to each other. The study addressed a subject that is currently raising much interest in ongoing research, *i.e.*, about the dynamic properties of masonry walls and how they change with damage. This research contributes to the knowledge on the dynamic behavior of masonry walls and highlights their complexity.

The modal frequencies obtained from the experimental data demonstrated the strengthening effects via the increase in structural frequencies for the second and third wall panels. When examining the changes in frequencies after cyclic tests, it was observed that the decrease in structural frequencies due to damage did not follow a consistent pattern. The amount or type of

damage observed could not be directly correlated with the decrease in frequencies. The study highlighted the complex dynamic behavior of masonry wall panels, which depend on multiple modes and various stiffness components. While a more detailed approach, such as measuring dynamic properties at each cycle, could potentially establish relationships between simple failure mechanisms and dynamic properties, it would require a significant number of experimental tests and analytical descriptions of specific failure modes, highlighting the need for further research. Furthermore, the dynamic properties of the wall panels differed due to the source of vibration used. The uncontrolled impact vibrations resulted in a decrease in frequencies due to increased damping in the masonry and its time-dependent behavior. Therefore, the study also underlined the challenges associated with *i*) experimental measurements, such as the effects of the vibration source on the identified parameters of masonry, *ii*) data processing that emphasized the difficulty of identifying mode shapes under heavy damage, *iii*) numerical modeling and the choice of modeling and updating parameters, *iv*) damage identification.

The analysis of mode shapes in the healthy state confirmed that the masonry walls are anisotropic and non-homogeneous, as expected. Damage in the walls increased the complexity of the problem and exacerbated the difficulty in detecting second and third mode shapes, which is attributed to existing cracks and discontinuities in the walls. Also, the presence of new local modes was attributed to severe damage occurred in the walls.

Advanced numerical modelling using DEM is intended to complement experimental findings where composite masonry texture is represented via a system of discrete blocks interacting through a recently developed elasto-softening contact model, including stiffness degradation. The adopted computational modeling strategy accurately captured the force-displacement behavior and the associated damage pattern of the benchmark wall under quasi-static loading, validating the accuracy of the model. However, comparisons between numerical and experimental dynamic properties highlighted deviations in modal properties, particularly for higher modes when monotonic loading (pushover analysis) was imposed. The predictions of the numerical model significantly improved when a cyclic material model and loading were used, but still a significant effort is required to predict the dynamic properties of the damaged state accurately. The authors acknowledge the availability of other advanced models and that different modeling strategies might become more suitable depending on the case tackled. Nonetheless, updating numerical models and considering linear and nonlinear parameters before and after damage were identified

as potential areas for improving the accuracy of modal property predictions in highly nonlinear structures like masonry walls.

While the study provided valuable insights into the dynamic behavior of masonry wall panels, further research is needed to explore the effects of damage on the dynamic properties of masonry walls, and to develop more accurate methodologies for characterizing modal properties in both the linear and nonlinear ranges. As presented and discussed throughout the paper, the prediction of the dynamic properties of the benchmark wall due to damage still needs improvement even though the nonlinear quasi-static behavior is very accurately captured. Therefore, only this simplest case has been studied and we refrained from analyzing more complex cases without ensuring a very good match in both linear and nonlinear domains for the benchmark wall. Modeling of more complex cases with wall strengthening as well as other wall dimensions and aspect ratios are identified as potential areas for future studies. Finally, this study raised more questions than it answered, albeit all relevant questions with the aim of developing a practical method for the vibration-based damage assessment of masonry structures.

5 Acknowledgments

The study is partially supported by Bogazici University Research Fund [grant number 12782].

6 References

[1] Gözde Çubuk E, Sayin E, Özmen A, Mühendisliği İ, Üniversitesi F, Fakültesi M, et al. Dynamic Analysis of Historical Masonry Arch Bridges under Different Earthquakes: The Case of Murat Bey Bridge. Turkish J Sci Technol 2022;17:461–73.

[2] Endo Y, Pelà L, Roca P, da Porto F, Modena C. Comparison of seismic analysis methods applied to a historical church struck by 2009 L'Aquila earthquake. Bull Earthq Eng 2015;13:3749–78. https://doi.org/10.1007/s10518-015-9796-0.

[3] Pulatsu B, Gonen S, Funari MF, Parisi F. Spatial stochastic D-RBA and limit equilibrium analysis of unreinforced masonry pier-spandrel structures. Eng Struct 2023;296:116897. https://doi.org/10.1016/j.engstruct.2023.116897.

[4] Gönen S, Soyöz S. Seismic analysis of a masonry arch bridge using multiple methodologies. Eng Struct 2021;226:111354. https://doi.org/10.1016/j.engstruct.2020.111354.

[5] Acikgoz S, DeJong MJ. The interaction of elasticity and rocking in flexible structures allowed to uplift. Earthq Eng Struct Dyn 2012;41:1–18. https://doi.org/10.1002/eqe.2181.

[6] Lourenço PB, Funari MF, Silva LC. Building resilience and masonry structures: How can computational modelling help? Comput Model Concr Concr Struct 2022:30–7. https://doi.org/10.1201/9781003316404-4.

[7] Funari MF, Spadea S, Lonetti P, Fabbrocino F, Luciano R. Visual programming for structural assessment of out-of-plane mechanisms in historic masonry structures. J Build Eng 2020;31:101425. https://doi.org/10.1016/j.jobe.2020.101425.

[8] Roca P, Cervera M, Gariup G, Pela' L. Structural Analysis of Masonry Historical Constructions. Classical and Advanced Approaches. Arch Comput Methods Eng 2010;17:299–325. https://doi.org/10.1007/s11831-010-9046-1.

[9] Parisi F, Lignola GP, Augenti N, Prota A, Manfredi G. Rocking response assessment of in-plane laterally-loaded masonry walls with openings. Eng Struct 2013;56:1234–48. https://doi.org/10.1016/j.engstruct.2013.06.041.

[10] Gönen S, Soyöz S. Reliability-based seismic performance of masonry arch bridges. Struct Infrastruct Eng 2022;18:1658–73. https://doi.org/10.1080/15732479.2021.1918726.

[11] Gonen S, Pulatsu B, Lourenço PB, Lemos J V., Tuncay K, Erduran E. Analysis and prediction of masonry wallette strength under combined compression-bending via stochastic computational modeling. Eng Struct 2023;278:1–36. https://doi.org/10.1016/j.engstruct.2022.115492.

[12] Anthoine, A.; Magonette, G.; Magenes G. Shear-compression testing and analysis of brick masonry walls. Proc. 10th Eur. Conf. Earthq. Eng., Vienna: 1995, p. 1657–62.

[13] Petry S, Beyer K. Influence of boundary conditions and size effect on the drift capacity of URM walls. Eng Struct 2014;65:76–88. https://doi.org/10.1016/J.ENGSTRUCT.2014.01.048.

[14] Almeida C, Guedes JP, Arêde A, Costa CQ, Costa A. Physical characterization and compression tests of one leaf stone masonry walls. Constr Build Mater 2012;30:188–97. https://doi.org/10.1016/J.CONBUILDMAT.2011.11.043.

[15] Vasconcelos G, Lourenço PB. In-Plane Experimental Behavior of Stone Masonry Walls under Cyclic Loading. J Struct Eng 2009;135:1269–77. https://doi.org/10.1061/(ASCE)ST.1943-541X.0000053.

[16] Tomazevic M. Some aspects of experimental testing of seismic behavior of masonry walls and models of masonry buildings. ISET J Earthq Technol 2000;37:101–17.

[17] Wilding BV, Dolatshahi KM, Beyer K. Shear-compression tests of URM walls: Various setups and their influence on experimental results. Eng Struct 2018;156:472–9. https://doi.org/10.1016/J.ENGSTRUCT.2017.11.057.

[18] Lourenço PB, Oliveira D V., Roca P, Orduña A. Dry Joint Stone Masonry Walls Subjected to In-Plane Combined Loading. J Struct Eng 2005;131:1665–73. https://doi.org/10.1061/(ASCE)0733-9445(2005)131:11(1665).

[19] Demir C. Seismic behaviour of historical stone masonry multi-leaf walls. Istanbul Technical University, 2012.

[20] Vasconcelos G, Lourenço PB. Experimental characterization of stone masonry in shear and compression. Constr Build Mater 2009;23:3337–45. https://doi.org/10.1016/J.CONBUILDMAT.2009.06.045.

[21] Calvi GM, Kingsley R, Magenes G. Testing of Masonry Structures for Seismic Assessment. Earthq Spectra 1996;12:145-162. https://doi.org/https://doi.org/10.1193/1.1585872.

[22] Doebling SW, Farrar CR, Prime MB. A summary review of vibration-based damage identification methods. Shock Vib Dig 1998;30:91–105. https://doi.org/10.1177/058310249803000201.

[23] Gentile C, Saisi A. Ambient vibration testing of historic masonry towers for structural identification and damage assessment. Constr Build Mater 2007;21:1311–21. https://doi.org/10.1016/J.CONBUILDMAT.2006.01.007.

[24] Clementi F, Formisano A, Milani G, Ubertini F. Structural Health Monitoring of Architectural Heritage: From the past to the Future Advances. Int J Archit Herit 2021;15:1–4. https://doi.org/10.1080/15583058.2021.1879499.

[25] Ubertini F, Comanducci G, Cavalagli N. Vibration-based structural health monitoring of a historic bell-tower using output-only measurements and multivariate statistical analysis. Struct Heal Monit 2016;15:438–57. https://doi.org/10.1177/1475921716643948.

[26] Kita A, Cavalagli N, Venanzi I, Ubertini F. A new method for earthquake-induced damage identification in historic masonry towers combining OMA and IDA. vol. 19. Springer Netherlands; 2021. https://doi.org/10.1007/s10518-021-01167-0.

[27] Ramos LF, Aguilar R, Lourenço PB. Operational modal analysis of historical constructions using commercial wireless platforms. Struct Heal Monit 2011;10:511–21. https://doi.org/10.1177/1475921710388973.

[28] Gonen S, Soyoz S. Dynamic identification of masonry arch bridges using multiple methodologies. Conf. Proc. Soc. Exp. Mech. Ser., Springer; 2021. https://doi.org/10.1007/978-3-030-47709-7_4.

[29] Gentile C, Saisi A. Operational modal testing of historic structures at different levels of excitation. Constr Build Mater 2013;48:1273–85. https://doi.org/10.1016/J.CONBUILDMAT.2013.01.013.

[30] Aytulun E, Soyoz S, Karcioglu E. System Identification and Seismic Performance Assessment of a Stone Arch Bridge. J Earthq Eng 2019;2469. https://doi.org/10.1080/13632469.2019.1692740.

[31] Costa C, Arêde A, Costa A, Caetano E, Cunha Á, Magalhães F. Updating Numerical Models of Masonry Arch Bridges by Operational Modal Analysis. Int J Archit Herit 2015;9:760–74. https://doi.org/10.1080/15583058.2013.850557.

[32] De Stefano A, Matta E, Clemente P. Structural health monitoring of historical heritage in Italy: some relevant experiences. J Civ Struct Heal Monit 2016;6:83–106. https://doi.org/10.1007/s13349-016-0154-y.

[33] Makoond N, Pelà L, Molins C, Roca P, Alarcón D. Automated data analysis for static structural health monitoring of masonry heritage structures. Struct Control Heal Monit 2020;27. https://doi.org/10.1002/stc.2581.

[34] Ramos LF, Aguilar R, Lourenço PB, Moreira S. Dynamic structural health monitoring of Saint Torcato church. Mech Syst Signal Process 2013;35:1–15. https://doi.org/10.1016/j.ymssp.2012.09.007.

[35] Demirlioglu K, Gonen S, Soyoz S, Limongelli MP. In-Plane Seismic Response Analyses of a Historical Brick Masonry Building Using Equivalent Frame and 3D FEM Modeling Approaches. Int J Archit Herit 2020;14:238–56. https://doi.org/10.1080/15583058.2018.1529208.

[36] Clementi F, Pierdicca A, Formisano A, Catinari F, Lenci S. Numerical model upgrading of a historical masonry building damaged during the 2016 Italian earthquakes: the case study of the Podestà palace in Montelupone (Italy). J Civ Struct Heal Monit 2017;7:703–17. https://doi.org/10.1007/s13349-017-0253-4.

[37] Di Primio A, Fiorini N, Spina D, Valente C, Vasta M. Ambient vibrations for the assessment of the strengthening intervention of a masonry barrel vault. Struct Heal Monit 2021;20:1312–30. https://doi.org/10.1177/1475921720952066.

[38] Gonen S, Soyoz S. Investigations on the elasticity modulus of stone masonry. Structures 2021;30:378–89. https://doi.org/10.1016/j.istruc.2021.01.035.

[39] ASTM E2126 - 11. Standard Test Methods for Cyclic (Reversed) Load Test for Shear Resistance of Vertical Elements of the Lateral Force Resisting Systems for Buildings. 2018.

[40] Gonen S, Pulatsu B, Erdogmus E, Lourenço PB, Soyoz S. Effects of spatial variability and correlation in stochastic discontinuum analysis of unreinforced masonry walls. Constr Build

Mater 2022;337. https://doi.org/10.1016/j.conbuildmat.2022.127511.

[41] Gonen S, Pulatsu B, Soyoz S, Erdogmus E. Stochastic discontinuum analysis of unreinforced masonry walls: Lateral capacity and performance assessments. Eng Struct 2021;238. https://doi.org/10.1016/j.engstruct.2021.112175.

[42] Garcia-Ramonda L, Pelà L, Roca P, Camata G. Cyclic shear-compression testing of brick masonry walls repaired and retrofitted with basalt textile reinforced mortar. Compos Struct 2022;283:115068. https://doi.org/10.1016/j.compstruct.2021.115068.

[43] Brincker R, Zhang L, Andersen P. Modal identification of output-only systems using frequency domain decomposition. Smart Mater Struct 2001;10:441–5. https://doi.org/10.1088/0964-1726/10/3/303.

[44] Brincker R, Ventura C, Andersen P. Damping estimation by frequency domain decomposition. 19th Int. Modal Anal. Conf., 2001.

[45] Allemang R, Brown D. A correlation coefficient for modal vector analysis. Proc. 1st Int. modal Anal. Conf., Orlando, Florida: 1982.

[46] Magalhães F, Cunha Á. Explaining operational modal analysis with data from an arch bridge. Mech Syst Signal Process 2011;25:1431–50. https://doi.org/10.1016/J.YMSSP.2010.08.001.

[47] Giordano E, Mendes N, Giovanna M, Clementi F, Haji N, André R, et al. Expeditious damage index for arched structures based on dynamic identification testing. Constr Build Mater 2020.

[48] Romanazzi A, Oliveira D V., Silva RA, Barontini A, Mendes N. Performance of rammed earth subjected to in-plane cyclic displacement. Mater Struct Constr 2022;55:1–17. https://doi.org/10.1617/s11527-022-01894-z.

[49] Hart R, Cundall PA, Lemos J V. Formulation of a three-dimensional distinct element model - Part II. Mechanical calculations for motion. Int J Rock Mech Min Sci Geomech 1988;25:117–25.

[50] Lemos J V. Discrete element modeling of masonry structures. Int J Archit Herit 2007;1:190–213. https://doi.org/10.1080/15583050601176868.

[51] Pulatsu B. Coupled elasto-softening contact models in DEM to predict the in-plane response of masonry walls. Comput Part Mech 2023. https://doi.org/10.1007/s40571-023-00586-x.

[52] Cundall P, Detournay C. Dynamic relaxation applied to continuum and discontinuum numerical models in geomechanics. Rock Mech Eng Vol 3 Anal Model Des 2017:45–90. https://doi.org/10.1201/b20402.

[53] Itasca Consulting Group Inc. 3DEC Three Dimensional Distinct Element Code 2013.

[54] Lourenço PB, Gaetani A. Recommended properties for advanced numerical analysis. Finite Elem. Anal. Build. Assess. Adv. Use Pract. Recomm., Routledge; 2022, p. 209–321. https://doi.org/10.31201/9780429341564-4.

[55] Makoond N, Cabané A, Pelà L, Molins C. Relationship between the static and dynamic elastic modulus of brick masonry constituents. Constr Build Mater 2020;259:120386. https://doi.org/10.1016/j.conbuildmat.2020.120386.